C. R. Mecanique 345 (2017) 35–46

Contents lists available at ScienceDirect

Comptes Rendus Mecanique

www.sciencedirect.com

Basic and applied researches in microgravity/Recherches fondamentales et appliquées en microgravité

Evaporation condensation-induced bubble motion after temperature gradient set-up

Vadim S. Nikolayev [a,*], Yves Garrabos [b], Carole Lecoutre [b], Guillaume Pichavant [c], Denis Chatain [c], Daniel Beysens [d,e]

[a] Service de physique de l'état condensé, CEA, CNRS, Université Paris-Saclay, CEA Saclay, 91191 Gif-sur-Yvette cedex, France
[b] CNRS, Université de Bordeaux, ICMCB, UPR 9048, 33600 Pessac, France
[c] Université Grenoble Alpes, CEA INAC–SBT, 38000 Grenoble, France
[d] Univ. Grenoble Alpes, CEA INAC–SBT, 38000 Grenoble, France
[e] ESEME, PMMH–ESPCI, 10, rue Vauquelin, 75231 Paris cedex 5, France

ARTICLE INFO

Article history:
Received 26 February 2016
Accepted 21 April 2016
Available online 31 October 2016

Keywords:
Bubble motion
Thermal gradient
Critical phenomena
Piston effect

ABSTRACT

Thermocapillary (Marangoni) motion of a gas bubble (or a liquid drop) under a temperature gradient can hardly be present in a one-component fluid. Indeed, in such a pure system, the vapor–liquid interface is always isothermal (at saturation temperature). However, evaporation on the hot side and condensation on the cold side can occur and displace the bubble. We have observed such a phenomenon in two different fluids submitted to a temperature gradient under reduced gravity: hydrogen under magnetic compensation of gravity in the HYLDE facility at CEA-Grenoble and water in the DECLIC facility onboard the ISS. The experiments and the subsequent analysis are performed in the vicinity of the vapor–liquid critical point to benefit from critical universality. In order to better understand the phenomena, a 1D numerical simulation has been performed. After the temperature gradient is imposed, two regimes can be evidenced. At early times, the temperatures in the bubble and the surrounding liquid become different thanks to their different compressibility and the "piston effect" mechanism, i.e. the fast adiabatic bulk thermalization induced by the expansion of the thermal boundary layers. The difference in local temperature gradients at the vapor–liquid interface results in an unbalanced evaporation/condensation phenomenon that makes the shape of the bubble vary and provoke its motion. At long times, a steady temperature gradient progressively forms in the liquid (but not in the bubble) and induces steady bubble motion towards the hot end. We evaluate the bubble velocity and compare with existing theories.

1. Introduction

Classically, when a bubble of gas (radius R) is immersed in a liquid and subjected to a temperature gradient, a bubble drift along the gradient is observed when the gravity effects are negligible. This motion is classically attributed to a thermocapillary (Marangoni) convection, the temperature gradient inducing a surface tension gradient that drives the flow. The bubble velocity in a steady gradient is given by the expression [1]

* Corresponding author.
E-mail address: vadim.nikolayev@cea.fr (V.S. Nikolayev).

http://dx.doi.org/10.1016/j.crme.2016.10.002

$$\vec{v}_M = -\frac{2}{2\eta_L + 3\eta_G}\frac{d\sigma}{dT}\frac{R}{2+\lambda_G/\lambda_L}\nabla T \tag{1}$$

Here T is temperature, ∇T is the temperature gradient, σ is surface tension, η_L and η_G are the liquid and gas shear viscosities and λ_L and λ_G are the liquid and gas thermal conductivities, respectively. Depending on the sign of $d\sigma/dT$, the gas bubble will move parallel or antiparallel to the thermal gradient. When both liquid and gas are the same substance, the gas corresponds to the pure vapor in equilibrium with its liquid. The vapor–liquid interface is at the saturation temperature. Any interface temperature change then leads to evaporation or condensation and will thus be immediately counterbalanced by the latent heat effect [2]. The thermocapillary motion is thus hardly possible. However, another reason for the bubble motion can exist.

A simple 1D model where the gradient is directed along the z direction shows that evaporation, which adds the vapor to the hot side of the bubble, and condensation, which removes it from the cold side, corresponds to a bubble drift with an (apparent) velocity v_D equal to the evaporation (condensation) interface velocity. The rate of evaporation dm/dt, where m is mass, t is time, S is the interface area perpendicular to z and L is the latent heat can be expressed as

$$\frac{dm}{dt} = Lv_D S\rho_L = \lambda_L S\frac{dT}{dz}. \tag{2}$$

Here ρ_L and ρ_V are the liquid and the vapor density, respectively. This gives the interface velocity

$$v_D = \frac{\lambda_L}{\rho_L L}\frac{dT}{dz}. \tag{3}$$

A similar reasoning applied to a 3D model (see Appendix A) results in a factor 3,

$$v_D = \frac{3\lambda_L}{\rho_L L}\frac{dT}{dz}. \tag{4}$$

In contrast to thermocapillary migration, the bubble always moves in the direction of the temperature gradient, with a constant speed independent of its radius. This approach was followed by Mok et al. [3] when analyzing their experiments in hydrogen H_2. The thermal gradient was used there to compensate buoyancy.

A further study was performed by Onuki and Kanatani [4] in the framework of a dynamic van der Waals theory starting with entropy and energy functional with gradient contributions [5]. The resultant hydrodynamic equations contain the stress arising from the density gradient. It provides a general scheme of two-phase hydrodynamics involving the vapor–liquid transition at non-uniform temperature. Accounting also for evaporation and condensation, the vapor bubble velocity v_D was found to be

$$v_D = \frac{\hat{\eta} + \left[(1+\hat{\eta}/2)\right]\hat{\rho}}{(1/3+\hat{\eta}/2)\,\rho_V L}\lambda_L \nabla T \tag{5}$$

where $\hat{\eta} = \eta_V/\eta_L$ and $\hat{\rho} = \rho_V/\rho_L$. Far from T_c ($\hat{\eta} \to 0$), this expression reduces to Eq. (4), which neglects however the hydrodynamic flow induced by the phase change. Note that close to T_c, where $\hat{\eta} \sim 1$ Eq. (5) yields exactly the same expression as $\hat{\rho} \sim 1$ in numerator and $\rho_V \sim \rho_L$ in denominator. This shows that the hydrodynamic flows caused by the phase transition have only a small impact on this phenomenon. They will be neglected in the theoretical part of the present article. The flow can however be important in constrained geometries (where the moving bubble size is comparable to the vessel size), as it will be discussed later on.

In this paper, we report preliminary experiments performed (i) with a H_2 vapor bubble in liquid H_2 under magnetic compensation of gravity near its critical point and (ii) in liquid–vapor water at saturation very near its critical point under weightlessness. The data are analyzed in the framework of a 1D model that ignores hydrodynamic effects, but captures the main characteristics of the problem, including phase change, release of latent heat and compressibility (piston effect). A realistic temperature distribution in the fluid is calculated. The bubble displacement caused by the evaporation/condensation process is evaluated, in particular at short times after temperature has been changed at the boundary, and late times when a steady gradient has taken place.

2. Experiment

2.1. Hydrogen under magnetic compensation of gravity

Gravity forces can be compensated by magnetic forces that are the strongest near the end of a solenoid. The HYLDE (HYdrogen Levitation DEvice) facility has been set up at CEA–Grenoble to work with hydrogen. Details can be found in [6]. It can be shown [7] that a perfect homogeneous acceleration field cannot be obtained in the whole volume. In practice, a zero value of effective gravity g^* is achieved at one or several points in space and can be made as small as needed within a finite volume by configuring the magnetic field [8]. When the condition $g^* = 0$ is achieved at some point, the spatial distribution of g^* is called “residual gravity”. The residual gravity is directed upward (downward) at the upper (lower) part of the cell, corresponding to bubble attraction to the cell center (i.e. to the stable position for bubble levitation at

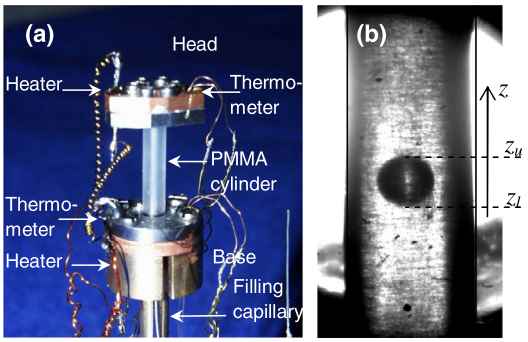

Fig. 1. The HYLDE cell. (a) Photo. (b) Observation of the bubble. The external diameter of the cylinder (4 mm) gives the scale.

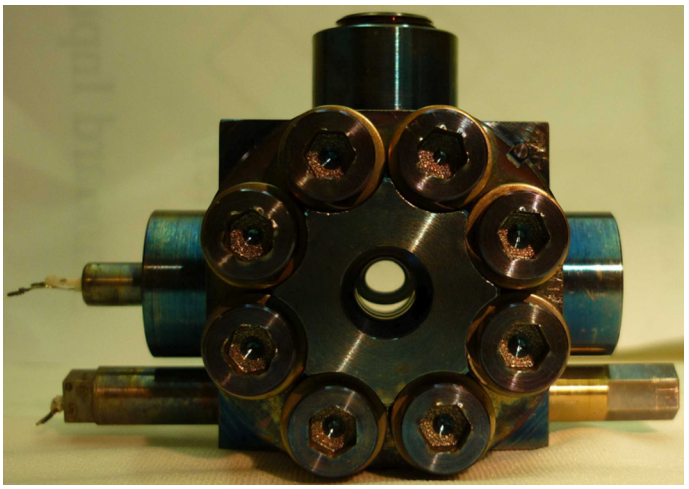

Fig. 2. Experimental cell for experiments with near critical pure water, in the High-Temperature Insert (HTI) inside the DECLIC facility.

equilibrium in the vertical direction). The radial variation of g^* corresponds to vapor repulsion from the coil axis. This is a severe limitation to study the long-term motion of bubbles, as the latter will always be trapped in some points of the cell. However, some qualitative observations can be made. Preliminary experiments have been performed in a cylinder of $L = 16.5$ mm in length, 3 mm in inner diameter, and 4 mm in outer diameter, made of polymethylmethacrylate (PMMA, denoted hereafter by the subscript S) (Fig. 1). The cylinder axis coincides with the magnetic coil axis. PMMA has been chosen because it is transparent and has a low thermal conductivity ($\lambda_S = 0.125$ W·m^{-1}·K^{-1} at 33 K) and the specific heat of the walls is low ($C_S = 180$ J·kg^{-1}·K^{-1} at 33 K). With a mass density of $1.15 \cdot 10^3$ kg·m^{-3}, one gets a thermal diffusivity $D_S = 6.04 \cdot 10^{-7}$ m^2·s^{-1}, corresponding to a characteristic diffusion time $t_S = L^2/D_S \simeq 400$ s. The PMMA cylinder is sealed with stainless steel rings to two parallel electrolytic copper (thermal conductivity at 33 K is ≈ 1130 W·m^{-1}·K^{-1}) blocks. They are in thermal contact with the helium bath by thermal conductors. Stainless steel is a thermal insulator at these low temperatures (thermal conductivity is 3.37 W·m^{-1}·K^{-1}). The upper copper block is called "head" (H). The other block is the "base" (B); it is kept at a constant temperature T_B with control accuracy ± 0.3 mK at 33 K; the working temperature range is 15–40 K. The cell can be filled with pure pressurized H_2 through a capillary. This capillary is closed by a H_2 ice plug (the H_2 solidification temperature is 14 K), whose formation is provided locally by a thermal conductor in contact with the helium bath. The cell is observed by coherent (parallel) light transmission (Fig. 1b). The cell is filled at the H_2 critical density.

The procedure consists in having initially base, head, fluid and cell walls at the same temperature. Then the base and/or the head temperature is changed by a given amount. Under gravitation compensation, weak thermal flows can appear when the head or the basis is heated due to the remaining gravity directed towards the cell center. When the head or the basis is cooled, such flows are not present.

2.2. DECLIC experiment

We briefly present here the optical cell for experimental observations of critical phenomena at high pressure and high temperature, using the HTI (High-Temperature Insert) module of the DECLIC instrument. DECLIC is the CNES–NASA joint project on board the International Space Station since 2009 [9]. A picture of the optical cell is given in Fig. 2, while details

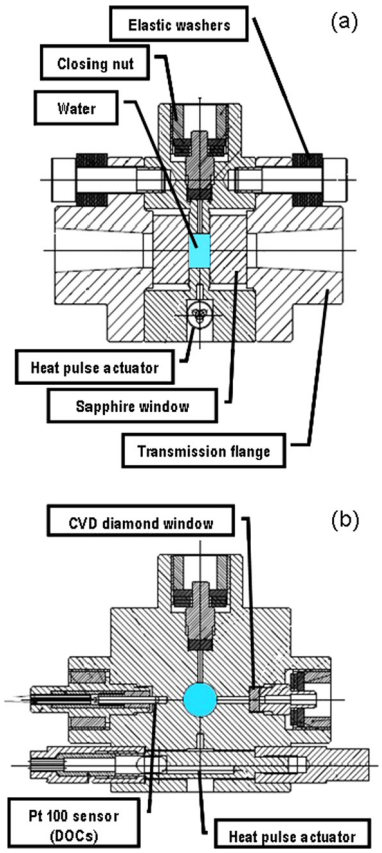

Fig. 3. (a) Side-view (with respect to Fig. 2) cross section of the HTI cell showing the optical channel for light transmission observation and details of the mechanical assembly. (b) Front-view cross section showing the optical channel for 90° light scattering measurements through the diamond window, and details of the Pt100 temperature sensor (DOCs).

can be found in [10]. High-resolution and high-speed optical diagnostics can be synchronized with temperature measurements and adjusted to the selected monitoring rate of the thermal pulses produced by one heating actuator. Temperature regulation is ensured to the sample cell unit that contains the high-pressure cell. Temperature is maintained constant within 0.5 mK around the critical point of water ($\approx$375 °C) and gradients of the order of 0.1 K·cm^{-1} can be created.

The cell design satisfies several scientific and safety requirements. The cell is intended to study water in the vicinity of its critical point using the optical diagnostics of the DECLIC instrument. The diagnostics methods include (coherent) light transmission, grid shadowgraphy of the complete cell volume, the turbidity measurements by laser light attenuation, static small angle light diffusion measurements, and 90° laser light scattering. For compatibility with the safety requirements of NASA on board the ISS, it can operate up to 405 °C and 33 MPa, and satisfies the leak-before-burst safety constraint. Both the cell body and the transparent materials need to be resistant to corrosion at high temperature, especially corrosion within supercritical water and aqueous media.

The transmission observation of the fluid volume can be made through a 8-mm observable diameter. In addition, 90° light scattering is measured by a photodiode through a 1.6-mm diameter. Several Pt sensors (resistance 25 Ω or 100 Ω) located in the cell body and its sample cell housing (SCH) are used to monitor temperature and/or to generate a heat flux close to the fluid.

Fig. 3a shows the cell and the cross-section of the fully assembled sample cell whose typical external dimensions are 62 mm in length, 55 mm in height, and 72 mm in depth. The cell body and transmission flanges are made of Inconel 718 (a nickel-based alloy manufactured by Aubert & Duval, France). The optical windows chosen for transmission observation are made of sapphire (18 mm in diameter, 9 mm in thickness), while the one for 90° light scattering measurements is made of synthetic bulk poly-crystalline diamond (5.5 mm in diameter, 1.2 mm in thickness). The thermal differential dilatation between different materials is accounted for by using an appropriate number of elastic washers made of Inconel 718 (from Ressorts Masselin, France). After filling at a near-critical density of water (quality Ultrex II, Ultrapure Reagent, from J.T. Baker, USA), the cell is closed by a “blind window” made of Inconel 718 (5.5 mm in diameter – 2.5 mm in thickness), using a similar design as the 90° light scattering part. The tightening is achieved using gold sealings.

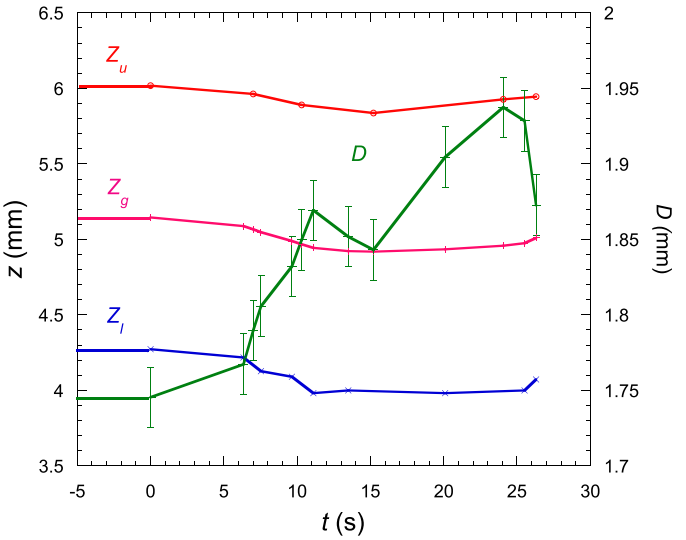

Fig. 4. Evolution of H_2 bubble upper and lower points (z_u and z_l, respectively), bubble mass center positions z_g (left ordinate axis) and bubble diameter $D = z_u - z_l$ (right ordinate axis). Initially, the base and the head temperatures are at $T_0 = 32.0$ K, then the base is cooled to $T_B = 31.8$ K.

The main volume (280 mm^3) of the fluid sample observed by transmission is a cylinder (8 mm in diameter, 5 mm in thickness), as shown in Fig. 3b. The dead volumes are limited to the small scattering and filling channels (1.6 mm and 1 mm in diameter, respectively, 7 mm in length). When filled at the critical density of water ($\rho_c = 322$ kg·m^{-3}), the mass of water is ≈90 mg.

The cell is integrated within a nickeled copper alloy housing (labeled SCH for Sample Cell Housing) to form the HTI Sample Cell Unit (SCU). The two Pt25 sensors used for temperature regulation (SCUr) and temperature measurements (SCUm) are located inside the copper alloy housing, while the Pt100 sensor used for temperature measurements (DOCs) inside the cell body is located in a channel in front of that used for 90° light scattering (see Fig. 3 for details). Temperature regulation (within ± 1 mK) is provided with two Peltier elements located symmetrically above and below the SCU.

Because of a disbalance of these Peltier elements, a temperature gradient was detected along the SCU axis. In order to compensate this effect, an additional temperature monitoring procedure has been implemented [10]. Based on the control of the gradient between the two Pt sensors located on both parts of the HTI cell inside the SCU, it allowed the temperature gradient through the cell to be minimized in nominal situations. This disbalance has also been used to impose a controlled temperature gradient perpendicular to the cell optical axis. This gradient could be varied by amplitude and by sign. Its typical amplitude was 1.6 K/m and the time to go from one steady gradient value to another one was about 3 h. We have taken advantage of it to carry out the experiments on the bubble drift.

Prior to any measurement, the critical temperature has been determined by visual observation of the onset of phase separation, resulting in the complete darkening of the cell (critical opalescence). The found value $T_c = (373.995 \pm 0.001)$ °C is in agreement with the preliminary determination at our ground-based laboratory. It is at present the most accurate determination of water critical temperature [11].

3. Measurement results

3.1. Hydrogen

In the adopted modus operandi, a steady temperature gradient is not established immediately after the head and/or the base temperature change. Initially, diffusive thermal layers develop inside the fluid near both the head and the base. The bulk temperature also changes, due to the pressure change in the bulk fluid. The temperature change is larger in the vapor bubble than in the liquid because the derivative $(\partial T/\partial p)_\rho$ is larger in the vapor phase than in the liquid phase [12]. The time scale of this pressure rise is quite small ("piston effect" [13]). This "piston effect" is all the more pronounced when the sample is closer to T_c. Thus a temperature gradient can immediately form near the liquid–vapor interface and causes a phase change that results in the modification of the bubble diameter and also its motion if the gradients around the bubble are not fully symmetric. In Fig. 4 is reported the bubble relaxation at $(T_0 - T_c)/T_c = 0.970$, $\nabla T = 0.129$ K/cm; the pressure drops, the bubble diameter increases, but the mean displacement of the center of mass, $z_g = (z_u + z_l)/2$ (z_u and z_l are the upper and lower points of the bubble, see Fig. 1b), remains negligible, in agreement with the formation around the bubble of piston-effect-induced symmetric temperature gradients.

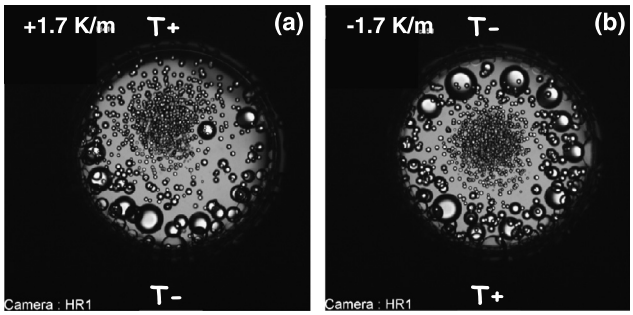

Fig. 5. Pattern of water bubbles ∼10,800 s ≈ 3 h after imposing a vertical temperature gradient of (a) 1.7 K/m and (b) −1.7 K/m at $T_c - 200$ mK. The mean displacement is ≈ 1 mm towards the hot end. The patterns look different because coalescence occurs during the bubble drift.

3.2. Water

The results on water are concerned with temperature gradients in two opposite directions along the SCU axis with a 1.7 K/m temperature gradient (Fig. 5). Note that this is the gradient imposed to the cell exterior. It has been observed that vapor bubbles always move towards the hotter side, as expected, with a velocity of about 0.37 mm/h ($1.02 \cdot 10^{-7}$ m·s^{-1}).

It is worth comparing the drift velocity value (4) with the experimental results. For water at $T_c - 200$ mK under a temperature gradient of ≈ 1.7 K·m^{-1}, where $L \approx 150$ kJ·kg^{-1}, $\lambda_L \approx 0.94$ W·m^{-1}·K^{-1}, and $\rho_L \approx 367$ kg·m^{-3}, one obtains $v \approx 0.29$ mm/h, which compares well with the above observation of the bubble drift of 0.37 mm/h. In addition, the displacement does not depend on the bubble size, which is in agreement with the underlying process of condensation/evaporation-induced displacement.

4. Theory

The experimental data are very difficult to be compared with the theoretical expression (4) because the experimental local value of the temperature gradient is unknown; one knows only the temperature difference of the cell ends and the cell length to calculate the average value of the gradient. In the vicinity of the critical point, thermal diffusion becomes very slow, so that the stationary temperature distribution is long to attain. In the near-critical region, the piston effect influences strongly the temperature variation in the cell. While the physical origin of the piston effect is well understood, the calculations required to represent realistic experimental conditions are difficult to carry out. The behavior of near-critical fluids is indeed complicated by the highly non-linear equations of state (EOS) used to describe them and because of the presence of the vapor–liquid interface, the position of which is *a priori* unknown and should be determined. Three theoretical approaches have been suggested for confined near-critical fluids in the absence of convection. The first is the hydrodynamic approach [13,14], which has been applied to our knowledge only to single-phase fluids. The second is the diffuse interface model approach [5]; only small size systems can be analyzed with it. Within the third ("thermodynamic") approach [15,16], the piston effect is taken into account by a supplementary term

$$g(T) = \left(1 - \frac{C_V}{C_P}\right)\left(\frac{\partial T}{\partial P}\right)_\rho \frac{\mathrm{d}P}{\mathrm{d}t} \tag{6}$$

introduced in the heat conduction equation as follows,

$$\frac{\partial T}{\partial t} = \frac{1}{\rho C_P}\nabla \cdot (\lambda \nabla T) + g(T) \tag{7}$$

where T is the local fluid temperature, C_V (C_P), the specific heat at constant volume (pressure). Note that the term $g(T)$ is important near the critical point where $C_P \gg C_V$. Eq. (7) is equivalent to the equations of the hydrodynamic approach if the time derivatives are replaced by the convective derivatives.

The bulk fluid motion is neglected and the pressure P, assumed to be homogeneous, is only a function of time. The pressure is determined from the fluid mass conservation and computed via the nonlinear expression [15]:

$$\frac{\mathrm{d}P}{\mathrm{d}t} = -\frac{\int_V (\partial\rho/\partial T)_P \, \partial T/\partial t \, \mathrm{d}V}{\int_V \rho \chi_T \, \mathrm{d}V} \tag{8}$$

where $\chi_T = \rho^{-1}(\partial\rho/\partial P)_T$ is the isothermal compressibility and V the volume of the fluid sample. The resolution of (8) requires an iterative procedure for each time step. It consists in calculating the temperature with Eqs. (6)–(7) for some trial value of P. The other thermodynamic parameters (ρ, χ_T, ...) are determining with the EOS

$$\Lambda(P, \rho, T) = 0 \tag{9}$$

Subsequent computation of the *volume* integrals in Eq. (8) gives a new value of $\mathrm{d}P/\mathrm{d}t$ from which the pressure P is corrected. The correction step is repeated until convergence. Such an approach has been used by several groups [17,18] in a 1D calculation for single-component (supercritical) fluids. The two-phase case has been solved within a similar approach in 1D [19,20]. The interface position was calculated from the heat balance at the vapor–liquid interface.

Such a method has proved to be efficient in 1D. However, its extension to higher dimensions would require a large computational effort. The computer resources would rise steeply because the thermodynamic variables would have to be evaluated at each grid point of the computational domain by means of an iterative procedure. The latter is necessary because the problem is nonlinear. The problem is still more difficult for two-phase fluids because of the *a priori* unknown interface position.

In [21], some of us proposed an approximate but more computationally efficient method for the calculation of heat and mass transfer in single-phase fluids. It was called "fast calculation method". It has been shown that, compared to the rigorous hydrodynamic approach, the fast method provides a sufficiently good accuracy. In the present work, it is generalized to the two-phase fluid case. It is then applied in 1D and its results are compared to the experimental data.

4.1. Fast calculation method

The method is based on the energy equation (7) with the initial condition of homogeneous temperature T_0 inside the fluid. It will be solved with the boundary element numerical method (BEM) [21], which uses only the values of the variables at the domain boundaries as unknowns. For this reason, it is far more efficient than the finite-difference method used previously for two-phase calculations [19,20]. However, this BEM advantage would be lost if the pressure equation in the form (8) were employed. Eq. (8) requires the knowledge of the variables at the internal domain points; they would need to be calculated anyway at each iteration from the boundary values (in a separate calculation). A different form of the pressure equation that uses only the boundary values of the variables thus needs to be derived. The thermodynamic approach will be used for its derivation. We summarize first the single-phase case [21].

4.1.1. Single-phase fluid

The total amount of heat δQ given to the fluid during the time δt can be calculated by integration over the external boundary S of the fluid,

$$\delta Q = \delta t \int_S j_n \,\mathrm{d}S \tag{10}$$

where j_n is the heat flux directed inwards to the fluid domain. According to a general thermodynamic expression,

$$\delta Q = \int_V \left[C_V \rho \left(\frac{\partial T}{\partial P}\right)_\rho \delta P - \frac{C_P}{\alpha_P}\delta\rho \right] \mathrm{d}V \tag{11}$$

where the integration is performed over the fluid volume V and

$$\alpha_P = -\frac{1}{\rho}\left(\frac{\partial \rho}{\partial T}\right)_P \tag{12}$$

is the isobaric thermal expansion coefficient. By applying the integral mean value theorem to (11), one finds

$$\delta Q = V C_V^{\mathrm{a}} \rho^{\mathrm{a}} \left(\frac{\partial T}{\partial P}\right)_\rho^{\mathrm{a}} \delta P \tag{13}$$

where the superscript 'a' means the value calculated for the average density ρ^{a} and the spatially homogeneous pressure P. The second term of (11) disappears after the averaging because the average density is constant (the fluid cell is closed) and $\delta\rho^{\mathrm{a}} \equiv 0$.

The single-phase version of the pressure equation is thus

$$\frac{\mathrm{d}P}{\mathrm{d}t} = \left(\frac{\partial P}{\partial T}\right)_\rho^{\mathrm{a}} \frac{1}{V\rho^{\mathrm{a}} C_V^{\mathrm{a}}} \int_S j_n \,\mathrm{d}S \tag{14}$$

The advantage of this form with respect to Eq. (8) is that it uses only the boundary and spatially averaged values.

The same idea of the volume averaging is applied to the energy equation where the term (6) is replaced by

$$g^{\mathrm{a}}(t) = \left(1 - \frac{C_V^{\mathrm{a}}}{C_P^{\mathrm{a}}}\right)\left(\frac{\partial T}{\partial P}\right)_\rho^{\mathrm{a}} \frac{\mathrm{d}P}{\mathrm{d}t} \tag{15}$$

and material parameters are replaced by their averaged values, which thus become independent of the spatial variable and depend only on time. The averaging permits to simplify Eq. (7) by introducing a variable

$$\psi(\vec{x},t) = T(\vec{x},t) - E^{\mathrm{a}}(P) \tag{16}$$

with $\vec{x}$ the position vector and

$$E^{\mathrm{a}}(P) = \int_{P_0}^{P} \left(1 - \frac{C_V^{\mathrm{a}}}{C_P^{\mathrm{a}}}\right) \left(\frac{\partial T}{\partial P}\right)_{\rho}^{\mathrm{a}} \mathrm{d}P + T_0 \tag{17}$$

where P_0 is the initial pressure related to the initial temperature T_0 through the EOS. The reason of the introduction of ψ is that it obeys a simpler equation

$$\frac{\partial \psi}{\partial t} = D^{\mathrm{a}} \nabla^2 \psi \tag{18}$$

with the trivial initial condition. The thermal diffusion coefficient $D^{\mathrm{a}} = \lambda^{\mathrm{a}}/\rho^{\mathrm{a}} C_P^{\mathrm{a}}$ depends on P only. This allows the time t to be replaced by a new independent variable τ defined by the equation

$$\frac{\mathrm{d}\tau}{\mathrm{d}t} = D^{\mathrm{a}}(P) \tag{19}$$

whose initial condition can be imposed as $\tau|_{t=0} = 0$. Since P is a function of t only, this initial value problem is fully defined. The substitution of Eq. (19) into Eq. (18) results in the linear diffusion problem

$$\begin{aligned} &\frac{\partial \psi}{\partial \tau} = \nabla^2 \psi \\ &\psi|_{\tau=0} = 0 \end{aligned} \tag{20}$$

It can be solved with BEM. A comparison with the rigorous hydrodynamic approach [21] shows that the fast method results in accurate calculations in spite of the simplifying assumptions.

4.1.2. Two-phase fluid

A similar approach can be used for the two-phase case. For the sake of generality, we perform the derivations for a case where N domains of one (liquid or vapor) phase denoted by the superscript $k = 1 \ldots N$ are surrounded by another (vapor or liquid, respectively) phase denoted by $k = N + 1$. The volume fractions corresponding to each of the domains can be introduced via

$$\phi^k = V^k/V \tag{21}$$

The fluid is assumed to be confined in a closed cell so that both the total volume and the total mass are conserved,

$$\sum_{k=1}^{N+1} \phi^k = 1 \tag{22}$$

$$\sum_{k=1}^{N+1} \phi^k \rho^k = \rho^{\mathrm{a}} \tag{23}$$

while both the average density ρ^k and the volume fraction ϕ^k of each domain may change in time due to phase change. By proceeding similarly to the single-phase case, one can apply the integral mean value theorem to (11), written for each domain,

$$\delta Q^k = V \phi^k \left[C_V^k \rho^k \left(\frac{\partial T}{\partial P}\right)_{\rho}^{k} \delta P - \frac{C_P^k}{\alpha_P^k} \delta \rho^k \right] \tag{24}$$

where the pressure is the same (because of its spatial homogeneity) for all domains. The upper index k means that the variable is calculated for the thermodynamic state defined by (ρ^k, P), i.e. they are spatially averaged. Unlike the single-phase case (cf. Eq. (13)), the second term does not disappear in Eq. (24) because $\delta\rho^k \neq 0$. Similarly to (10), the δQ^k values can be obtained by integration over the boundary S^k of the k-th domain,

$$\delta Q^k = \delta t \int_{S^k} j_n^k \, \mathrm{d}S \tag{25}$$

where j_n^k is the heat flux along the vector normal to S^k and directed inwards to the k-th domain, $k = 1 \ldots N + 1$.

A part of the heat supplied to the fluid is used for evaporation or condensation at each of the interfaces. As in previous works [19,20], it is assumed that the phase transition does not occur inside the domains so that the liquid can be overheated

and vapor subcooled there. This hypothesis can be checked easily *a posteriori* by comparing the maximum overheating or subcooling to the typical nucleation barrier values. The heat amount

$$\delta Q_i^k = -\delta t \int_{S^k} (j_n^k + j_n^{N+1})\,\mathrm{d}S \tag{26}$$

is consumed at the k-th internal vapor–liquid interface, so that

$$\delta Q_i^k = \mp V L \delta(\rho^k \phi^k) \tag{27}$$

where $\mathcal{L}$ is the latent heat. The upper sign corresponds to a case where the domains $k = 1 \ldots N$ are liquid and the domain $N+1$ is the vapor; the lower sign refers to the opposite situation. By combining Eqs. (26) and (27), one obtains

$$\pm L \frac{\mathrm{d}(\rho^k \phi^k)}{\mathrm{d}t} = \frac{1}{V} \int_{S^k} (j_n^k + j_n^{N+1})\,\mathrm{d}S \tag{28}$$

where $k = 1 \ldots N$. Similarly, Eq. (24) combined with (25) results in

$$\phi^k \left[C_V^k \rho^k \left(\frac{\partial T}{\partial P} \right)_\rho^k \frac{\mathrm{d}P}{\mathrm{d}t} - \frac{C_P^k}{\alpha_P^k} \frac{\mathrm{d}\rho^k}{\mathrm{d}t} \right] = \frac{1}{V} \int_{S^k} j_n^k \,\mathrm{d}S \tag{29}$$

where $k = 1 \ldots N+1$. We obtain a set of $2N+1$ ordinary differential equations (ODE): N equations (28), and $N+1$ equations (29). Two conservation laws ((22), (23)) can be used to eliminate ϕ^{N+1} and ρ^{N+1} variables from the last of equations (29). This set of $2N+1$ equations is linear with respect to the $2N+1$ time derivatives of ϕ^k, ρ^k, and P. The set can thus be easily solved with respect to the derivatives, either numerically or analytically. The resulting set of $2N+1$ ODE in the canonic form can be solved at each iteration step by any numerical method, like that of Runge–Kutta.

The equations for the reduced temperature ψ^k in the k-th domain are similar to Eqs. (16)–(20), where the superscript a need to be replaced by k; note that τ^k will also be different for each domain. In addition to the boundary conditions at the external surface of the fluid, extra conditions are necessary at the vapor–liquid interfaces. The pressure fixes there the temperature to be equal to the saturation temperature $T_{\mathrm{sat}} = T_{\mathrm{sat}}(P)$. At the interfaces S^k, the conditions for ψ read

$$\psi^{N+1} + E^{N+1} = \psi^k + E^k = T_{\mathrm{sat}}(P) \tag{30}$$

where $k = 1 \ldots N$.

4.2. Problem statement

Usually, the "temperature step" boundary condition is applied for 1D problems. This heating process corresponds to a fluid cell, initially at uniform temperature, which is submitted to sudden temperature increase ΔT at one of its boundaries, while the other is kept at the initial temperature T_0. This heating condition is physically unrealistic because the initial value for the heat flux at the heated boundary is infinite. In this work, we use instead the gradual temperature increase,

$$T_{\mathrm{H}} = T_0 + \Delta T\,[1 - \exp(-t/\tau_r)] \tag{31}$$

where τ_r is the transition time.

4.3. 1D numerical results

We report the 1D simulation of the behavior of a H_2 bubble of size $D = 2.1$ mm initially located in the middle of the cell. The theory is quite general and can be applied to both liquid drops and vapor bubbles. For practical reasons (the container walls are in general wetted by liquid), bubble motion inside the liquid is often considered. The cell is initially at $T_0 = 0.875\,T_{\mathrm{c}}$ (28.875 K). At time $t = 0$, the temperature of the head located at $z = 16.5$ mm is changed to $T_0 + \Delta T = 0.945\,T_{\mathrm{c}}$ (31.185 K), with typical time $\tau_r = 1$ s, while the base temperature $T_{\mathrm{B}} \equiv T(z = 0) = T_0$. Two time regions can be evidenced with respect to the thermal diffusion time, $t_{\mathrm{D}} = L^2/D^{\mathrm{a}} \approx 450$ s. The 1D simulation seems to be sufficient for the following reasons. The lateral PMMA cell walls have a small thermal conductivity similar to that of the liquid and of the vapor. The exterior of the cell is under vacuum and the radiation heat losses are low because of low temperatures; the exterior of the cell is thus adiabatic, and radial thermal gradients are not expected.

4.3.1. Short times

When T_{H} is raised, the temperature profile is soon modified as seen in Fig. 6a. First, a hot thermal boundary layer develops at the hot end while, thanks to the piston effect, the bulk temperature and sample pressure increase homogeneously. This temperature increase is much more pronounced in the vapor phase because the term g is much larger there [12]. This creates hot boundary layers close to the bubble interface. The weak recondensation process occurs and the bubble volume

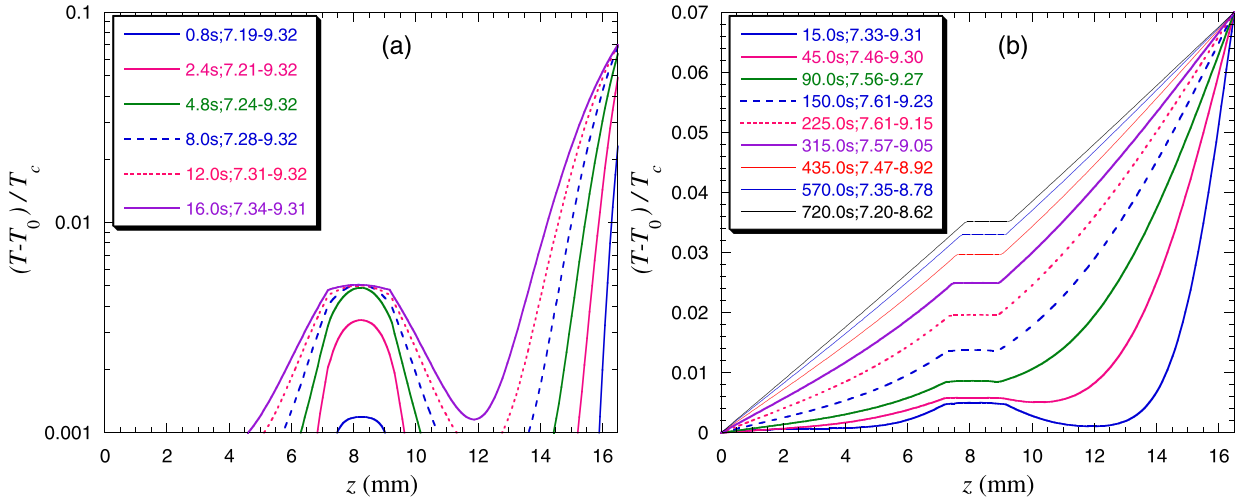

Fig. 6. Simulated evolution of the spatial temperature distribution in the 1D cell. The curve legends show the corresponding times and positions of the lower and upper bubble ends (in mm). (a) Short times (semi-log plot). (b) Long times.

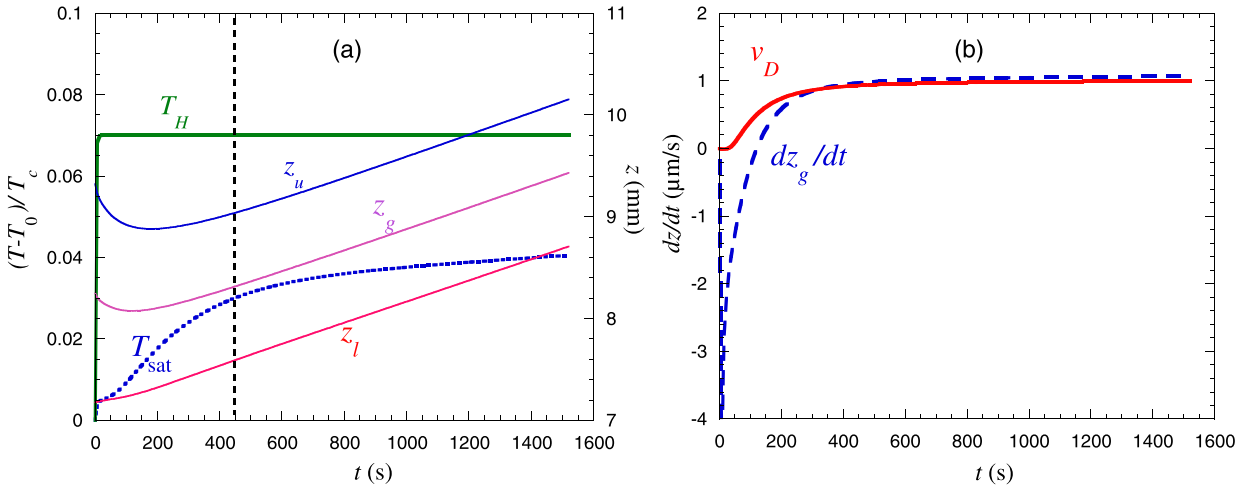

Fig. 7. (a) Simulated evolution of the interface temperature and the location of interfaces z_l, z_u and $z_g = (z_l + z_u)/2$. (b) Corresponding velocity dz_g/dt (interrupted curve) as compared to the velocity v_D (full curve) calculated with Eq. (3).

decreases. The dynamics of the center of mass of bubble is determined by the recondensation process, i.e. by the asymmetry of the temperature distribution around the bubble. The bubble slightly displaces to the cold end of the cell (Fig. 7).

The short-time behavior of the H_2 bubble (motion and bubble shrinking immediately after heating) can thus be satisfactorily explained by the short-time transient behavior.

4.3.2. Long times

As time goes on, the hot boundary layer developed at the hot end attains the bubble. The mass transfer inverses the sign and the evaporation begins at the hot end of the bubble, while condensation continues at its cold end. As the temperature profile develops towards a linear profile, both interfaces start to move with the same velocity in the same (hot) direction, resulting in a constant bubble size. Fig. 6b and Fig. 7a show this behavior, where a constant shape and constant velocity are observed for times longer than the diffusion time (≈ 450 s). It is interesting to compare the value of this asymptotic velocity with that obtained from Eq. (3), where the value of the gradient is taken as an average of the gradients at the bubble interface. The comparison needs to be made with Eq. (3), which is suitable for the 1D case, rather than with Eq. (4), derived for the 3D case (see Appendix A). The agreement is satisfactory at long times where the piston effect is negligible.

Only the case of the non-symmetric initial temperature change is simulated here. In the case of the symmetric temperature change, the piston effect is not expected to be pronounced, and the bubble will not move or change its size until the diffusive boundary layer attains it. In other words, the bubble is expected to remain still and unchanged at short time scale; its behavior is expected to be similar to the above-simulated case at long times.

5. Concluding remarks

A gas bubble immersed in a liquid submitted to a temperature gradient is usually assumed to move because of the interfacial tension variation along its interface. When the gas is the pure vapor of the same fluid, the interface has to be isothermal at the saturation temperature and thermocapillary motion should not occur. However, evaporation on the hot side and condensation on the cold side can occur and indeed displace the bubble. Experiments performed under weightlessness to cancel the buoyancy effects with water near its critical point (≈647 K) have confirmed this behavior. Another series of experiments with hydrogen near its critical point (≈ 33 K) under magnetic compensation of gravity shows transient behavior. The latter involves complicated interplay of pressure change due to piston effect, release of latent heat and thermal diffusion, and can be well understood by 1D numerical simulations. That method of simulations, which has been previously validated for the supercritical (single phase) fluids, has been extended here for the two-phase fluid case. Compared with the existing methods, the present method requires much smaller computation resources and is thus suitable for simulations in higher dimensions in the absence of gravity.

Acknowledgements

This work was supported in part by CNES MFA program. We are grateful to C. Mariette for helpful comments and thank CNES and NASA for having provided us the access to the International Space Station.

Appendix A. 3D bubble drift in a constant temperature gradient model

Consider a spherical bubble of radius R in an externally imposed constant temperature gradient $\mathrm{d}T/\mathrm{d}z$. The bubble interface with the imposed saturation temperature (with respect to which T will be given) will perturb the linear temperature field. The solution to the overall field is given in [22] (problem 1 of Sec. 3) for the case when the bubble center is momentarily situated at $z = 0$ point, where the unperturbed value of the temperature $T = 0$ (this assumption does not lead to the loss of generality). In the spherical reference ($z = r\cos\theta$)

$$T = r\frac{\mathrm{d}T}{\mathrm{d}z}\cos\theta(1 - R^3/r^3) \tag{A.1}$$

The local velocity of the bubble surface due to evaporation–condensation is found from the heat flux j_n,

$$v_n(\theta) = \frac{j_n}{\rho_\mathrm{L} L} = \frac{\lambda_\mathrm{L}}{\rho_\mathrm{L} L}\left.\frac{\mathrm{d}T}{\mathrm{d}r}\right|_{r=R} = \frac{3\lambda_\mathrm{L}}{\rho_\mathrm{L} L}\frac{\mathrm{d}T}{\mathrm{d}z}\cos\theta \tag{A.2}$$

Since the position of the mass center of the bubble is defined by

$$z_g = \frac{1}{V_\mathrm{b}}\int_{V_\mathrm{b}} z\,\mathrm{d}V$$

where $V_\mathrm{b} = 4\pi R^3/3$ is the bubble volume, the bubble velocity is

$$v_\mathrm{D} = \frac{\mathrm{d}z_g}{\mathrm{d}t} = \frac{1}{V_\mathrm{b}}\frac{\mathrm{d}}{\mathrm{d}t}\int_{V_\mathrm{b}} z\,\mathrm{d}V - \frac{1}{V_\mathrm{b}}\frac{\mathrm{d}V_\mathrm{b}}{\mathrm{d}t}z_g$$

The second term disappears since $z_g = 0$ according to our initial assumption.

By using the Reynolds transport theorem, one obtains

$$v_\mathrm{D} = \frac{1}{V_\mathrm{b}}\int_{S_\mathrm{b}} z\,v_n\,\mathrm{d}S \tag{A.3}$$

where v_n from Eq. (A.2) has to be used. The integration over the bubble surface S_b can be reduced to that over θ that varies from 0 to π, $\mathrm{d}S = 2\pi R^2\sin\theta\,\mathrm{d}\theta$. By carrying out the integration, one recovers Eq. (4).

References

[1] N.O. Young, J.S. Goldstein, M.J. Block, The motion of bubbles in a vertical temperature gradient, J. Fluid Mech. 6 (1959) 350–356, http://dx.doi.org/10.1017/S0022112059000684.

[2] Y. Garrabos, C. Lecoutre-Chabot, J. Hegseth, V.S. Nikolayev, D. Beysens, J.-P. Delville, Gas spreading on a heated wall wetted by liquid, Phys. Rev. E 64 (5) (2001) 051602, http://dx.doi.org/10.1103/PhysRevE.64.051602.

[3] L. Mok, K. Kim, T.P. Bernat, D.H. Darling, Temperature effects on the formation of a uniform liquid layer of hydrogen isotopes inside a spherical cryogenic ICF target, J. Vac. Sci. Technol. A 1 (2) (1983) 897–900, http://dx.doi.org/10.1116/1.572146.

[4] A. Onuki, K. Kanatani, Droplet motion with phase change in a temperature gradient, Phys. Rev. E 72 (6) (2005) 066304, http://dx.doi.org/10.1103/PhysRevE.72.066304.

[5] A. Onuki, Dynamic van der Waals theory, Phys. Rev. E 75 (3) (2007) 036304, http://dx.doi.org/10.1103/PhysRevE.75.036304.
[6] R. Wunenburger, D. Chatain, Y. Garrabos, D. Beysens, Magnetic compensation of gravity forces in (p-)hydrogen near its critical point: application to weightless conditions, Phys. Rev. E 62 (1) (2000) 469–476, http://dx.doi.org/10.1103/PhysRevE.62.469.
[7] L. Quettier, H. Félice, A. Mailfert, D. Chatain, D. Beysens, Magnetic compensation of gravity forces in liquid/gas mixtures: surpassing intrinsic limitations of a superconducting magnet by using ferromagnetic inserts, Eur. Phys. J. Appl. Phys. 32 (3) (2005) 167–175, http://dx.doi.org/10.1051/epjap:2005074.
[8] V. Nikolayev, D. Chatain, D. Beysens, G. Pichavant, Magnetic gravity compensation, Microgravity Sci. Technol. 23 (2) (2011) 113–122, http://dx.doi.org/10.1007/s12217-010-9217-6.
[9] R. Marcout, G. Raymond, B. Martin, G. Cambon, B. Zappoli, F. Duclos, S. Barde, D. Beysens, Y. Garrabos, C. Lecoutre, B. Billia, N. Bergeon, N. Mangelinck, DECLIC: a facility to investigate fluids and transparent materials in microgravity conditions in ISS, in: Proc. 56th Int. Astronautical Congress, Valencia, Spain, 2006, paper IAC-06-A2.5.02.
[10] G. Pont, S. Barde, P. Bioulez, D. Blonde, B. Zappoli, Y. Garrabos, C. Lecoutre, D. Beysens, N. Bergeon, L. Billia, N. Mangelinck-Noël, A. Ramirez, R. Trivedi, DECLIC, first result on orbit, in: Proc. 61st Int. Astronautical Congress, Prague, Czech Republic, 2010, paper IAC-10-A2.5.1.
[11] W. Wagner, A. Pruss, The IAPWS formulation 1995 for the thermodynamic properties of ordinary water substance for general and scientific use, J. Phys. Chem. Ref. Data 31 (2) (2002) 387–535, http://dx.doi.org/10.1063/1.1461829.
[12] R. Wunenburger, Y. Garrabos, C. Lecoutre-Chabot, D. Beysens, J. Hegseth, Thermalization of a two-phase fluid in low gravity: heat transferred from cold to hot, Phys. Rev. Lett. 84 (18) (2000) 4100–4103, http://dx.doi.org/10.1103/PhysRevLett.84.4100.
[13] B. Zappoli, D. Beysens, Y. Garrabos, Heat Transfer and Related Phenomena in Supercritical Fluids, Springer, Berlin, Heidelberg, ISBN 978-94-017-9186-1, 2015.
[14] B. Zappoli, D. Bailly, Y. Garrabos, B. Le Neindre, P. Guenoun, D. Beysens, Anomalous heat transport by the piston effect in supercritical fluids under zero gravity, Phys. Rev. A 41 (4) (1990) 2264–2267, http://dx.doi.org/10.1103/PhysRevA.41.2264.
[15] H. Boukari, J.N. Shaumeyer, M.E. Briggs, R.W. Gammon, Critical speeding up in pure fluids, Phys. Rev. A 41 (4) (1990) 2260–2263, http://dx.doi.org/10.1103/PhysRevA.41.2260.
[16] D. Beysens, D. Chatain, V.S. Nikolayev, J. Ouazzani, Y. Garrabos, Possibility of long-distance heat transport in weightlessness using supercritical fluids, Phys. Rev. E 82 (6) (2010) 061126, http://dx.doi.org/10.1103/PhysRevE.82.061126.
[17] J. Straub, L. Eicher, A. Haupt, Dynamic temperature propagation in a pure fluid near its critical point observed under microgravity during the German Spacelab Mission D-2, Phys. Rev. E 51 (6) (1995) 5556–5563, http://dx.doi.org/10.1103/PhysRevE.51.5556.
[18] F. Zhong, H. Meyer, Density equilibration near the liquid-vapor critical point of a pure fluid: single phase $T > T_c$, Phys. Rev. E 51 (4) (1995) 3223–3241, http://dx.doi.org/10.1103/PhysRevE.51.3223.
[19] J. Straub, L. Eicher, Density and temperature relaxation in the two-phase region near the critical point of a pure fluid, Phys. Rev. Lett. 75 (8) (1995) 1554–1557, http://dx.doi.org/10.1103/PhysRevLett.75.1554.
[20] F. Zhong, H. Meyer, Density equilibration near the liquid-vapor critical point of a pure fluid. II. Coexisting phases for $T < T_c$, Phys. Rev. E 53 (6) (1996) 5935–5948, http://dx.doi.org/10.1103/PhysRevE.53.5935.
[21] V.S. Nikolayev, A. Dejoan, Y. Garrabos, D. Beysens, Fast heat transfer calculations in supercritical fluids versus hydrodynamic approach, Phys. Rev. E 67 (6) (2003) 061202, http://dx.doi.org/10.1103/PhysRevE.67.061202.
[22] L.D. Landau, E.M. Lifshitz, Electrodynamics of Continuous Media, 2nd ed., Pergamon Press, Oxford, UK, 1963.